Locally Optimized Chirplet Spectrogram for Condition Monitoring of Induction Machines in Transient Regime

J. Martinez-Roman, R. Puche-Panadero, A. Sapena-Bano, J. Burriel-Valencia, M. Riera-Guasp, and M. Pineda-Sanchez*

Institute for Energy Engineering, Universitat Politècnica de València, Camino de Vera s/n, 46022, Valencia, Spain

Abstract

The locally optimized chirplet spectrogram (LOCS) is a novel method proposed in this work for generating a high-resolution and cost-effective spectrogram of the induction machine (IM) current, suitable for the identification of fault-related harmonics in transient conditions. Its distinctive novelty is that it optimizes automatically the parameters of the analysing window used for building the current spectrogram, at each point of the time-frequency plane, with the computational cost of a conventional, non-optimized spectrogram. It is based on the definition of a large dictionary of different chirplet windows, which are combined into a single, complex time window. A single short time Fourier transform with this new window generates in parallel the spectrograms of all the dictionary windows, and the LOCS chooses among them the locally optimized values in an automatic way. The proposed technique is applied to the diagnosis of two commercial induction motors with bar breakages and mixed eccentricity faults.

Keywords: Fault diagnosis, Fourier transforms, induction machines,

spectrogram, condition monitoring

1. Introduction

Induction machines (IMs) are the main mechanical power source of many industrial processes, specially squirrel cage motors [1, 2], and are also an important source of power supply networks, specially double fed induction wind generators (DFIGs) [3]. Their failure means an interruption of these power sources, which may lead to sudden stoppage of production lines and may cause high economic losses. To ensure their reliable operation, it is necessary to detect their faults at an early stage [4, 5, 6, 7], what allows taking corrective measures before the fault becomes a catastrophic one. Different condition based maintenance systems (CBMS) for IMs have been described in the technical literature [8], based on vibrations [9], sound analysis [10, 11], thermal signals [12], etc. Among them, motor current signature analysis (MCSA) [13, 14, 15, 16] has gained an increasing interest, because it can operate on-line, detecting different and possibly simultaneous types of fault, and can be implemented using non-invasive [17] low-cost current sensors, and fast processing algorithms, especially the fast Fourier transform (FFT). MCSA is based on the detection of a set of harmonic components generated by each type fault, whose frequencies constitute a unique fault signature [18]. These frequencies, for some of the most frequent IM faults [19], are given in Table 1, where p is the number of pole pairs, f_1 is the supply frequency, s is the rotor slip, and N_b, D_b, D_c and β are the parameter of the bearing (number of balls, bearing and cage diameter, and contact angle, respectively).

In spite of its simplicity, the industrial application of MCSA may have serious drawbacks. In particular, the fault frequencies given in Table 1 depend on the machine speed (through the slip), and on the supply frequency. Therefore, in many industrial processes that operate under varying load or speed conditions, as in the case of wind generators with variable wind regimes, the fault frequencies shown in Table 1 are not constant, and the fault signatures are not single spectral

2

Table 1: Frequencies of the Current Components Generated by Different Types of IM Faults

Type of fault	Frequency of the Fault Components	
Shorted coils [20]	$f_1 \cdot \left| k \pm n\frac{1-s}{p} \right|$	$k = 1, 3, 5 \ldots$ $n = 1, 2, 3, \ldots$
Rotor asymmetries [21, 22]	$f_1 \cdot (1 \pm 2ks)$	$k = 1, 2, 3 \ldots$
Mixed eccentricity [23]	$f_1 \cdot \left| 1 \pm k\frac{1-s}{p} \right|$	$k = 1, 2, 3 \ldots$
Bearing (outer race) [24, 25]	$\frac{N_b}{2}\frac{1-s}{p}f_1 \cdot \left[1 - \frac{D_b \cos(\beta)}{D_c} \right]$	
Bearing (inner race) [24, 25]	$\frac{N_b}{2}\frac{1-s}{p}f_1 \cdot \left[1 + \frac{D_b \cos(\beta)}{D_c} \right]$	
Bearing (balls) [26]	$f_1 \cdot \left| \frac{1}{2D_b}D_c\frac{1-s}{p}f_1\left[1 - \left(\frac{D_b \cos(\beta)}{D_c} \right)^2 \right] \right|$	

lines [27], which makes their identification very difficult. This fact limits the use of the FFT in MCSA to machines working in steady-state conditions.

To overcome this limitation, the FFT must be replaced by advanced time-frequency (TF) transforms that can display the energy content of the current in the TF plane, where the fault harmonics can be accurately detected, even under transient conditions. Different TF transforms have been proposed for fault diagnosis of IMs, such as the short-time Fourier transform (STFT) [6, 28, 29], the Stockwell transform [30], the Wigner-Ville distribution (WVD) [31], the wavelet transform (WT) [32], the spectral graph wavelet transform (SGWT) [33], or the continuous complex wavelet transform (CCWT) [34], among many others. In this work, the STFT has been selected, being a linear transform that does not generate cross-terms artefacts.

The current spectrogram generated by the STFT relies on windowing the current signal, at every time instant, and obtaining the FFT of this windowed

3

signal. The resolution of the spectrogram depends on the type and on the parameters of the window, and is limited by the uncertainty principle. The Gaussian window is the only one that reaches this limit [35], what justifies its selection in this work. Another factor that affects the capability of the spectrogram for displaying the current components is their degree of overlapping with the analysing window. To maximize it, the frequency-to-time ratio of the Gaussian window must coincide with the rate of change of the frequencies of these components [36]. An improvement of this approach is the possibility of rotating the analysing window in the TF plane, using a window with linearly varying frequency (chirplet), as in the chirplet transform (CT) [37, 38, 39, 40]. The extra degree of freedom given by the angle of rotation of the chirplet window allows achieving a better overlap with the fault harmonic and, therefore, a better spectrogram resolution. The CT has been used for detecting bearing faults in [41, 42], rotor imbalances in [43], and for detecting the rotating frequency from the vibration signal in [44]. The CT has also been applied to the analysis of the start-up transient of an IM in [45] for bearing fault detection, for rotor fault diagnosis in [46], and for eccentricity fault diagnosis in [47]. In [48], a variational non-linear component decomposition (VNCD) is proposed to overcome the limitations of the variational nonlinear chirp mode decomposition (VNCMD), which requires a prior knowledge that limits its practical application.

Maximizing, at each point of the TF plane, the overlap between the analysing window and the fault components of the current requires a thorough evaluation of their expected trajectories in this plane [47]. To avoid this process, an alternative approach is the post-processing of the current spectrogram, concentrating the energies of their elements in the most prominent ones, either by reassignment [49, 50], synchrosqueezing [51, 52] or synchroextraction [53] techniques. In [54] an enhanced post-processing method applied to the mono-components signals extracted using he instantaneous frequency has been proposed to detect misalignments of the outer and inner race of the bearings of an induction motor. These techniques help improve the contrast of the spectrogram, but their computational cost is very high. Instead, other authors propose the generation

4

of a set of different spectrograms, using different windows stored in a dictionary [55], as in the matching pursuit approach [56], or in the locally optimized spectrogram proposed in [57], using a fractional Fourier transform. For each TF position, the maximum value computed with all the different spectrograms is chosen to represent the energy content of the current signal at that point. This method has the advantage of not needing an a priori estimation of the fault harmonics trajectories. Nevertheless, its computational burden may be very high: a different spectrogram must be built for each analysing window, which, depending on the size of the dictionary, can be computationally very costly. That imposes a limit to the size of the dictionary, and thus to the resolution of the current spectrogram.

To avoid the use of windows dictionaries, an alternative approach consists in using different windows in different zones of the TF plane. The WT achieves a multi-resolution analysis by shifting and scaling a mother wavelet. The WT has been used for the diagnosis of electrical machines in [58], using the discrete WT (DWT) with a Daubechies wavelet, in [59], using the dual tree complex WT (DTCWT), and in [60] using the empirical WT (EWT). Nevertheless, the dyadic nature of the DCTWT or the scaling frequency of the WT are not well adapted to represent accurately the TF trajectories of the current components.

To overcome these limitations, this paper introduces a new method designated as "local optimized chirplet transform" (LOCS). This name refers to one of the outstanding characteristics of the new method, which consists in that it automatically selects the parameters of the analysis window that optimize the extraction of the fault components, at each point of the time-frequency plane. Furthermore, this optimization process does not increase the computational costs compared with conventional TF transforms, in which the chirplet parameters are constant throughout the TF plane. The LOCS defines a large number of chirplet windows, with different parameters, and combines them into a single, complex time window, as in [61]. In this way, it can perform the chirplet transform of the current signal using a high number of chirplet windows in the dictionary, while keeping an extremely low computing cost, similar

5

to the cost of computing a conventional, non-optimized spectrogram, based on a single window. It is based on:

1. Building a dictionary of chirplet windows with a wide range of rotation angles.

2. Combining all these windows into a single, complex time window, using non-overlapping frequency bands. A single run of the STFT algorithm using this novel complex window gives, in parallel, as many spectrograms as the number of windows in the dictionary. This feature makes the LOCS approach especially well-suited for embedded diagnostic systems of IMs working under transient conditions, such as modern field diagnostic devices that are physically attached to the machine core, and have a limited computing power.

3. As no previous knowledge is required about the expected signatures of the current components, the process can be fully automated, making it suitable for implementing artificial intelligence diagnostic systems for IMs.

Up the best of the authors' knowledge, it is the first time in the technical literature that a complex time window has been proposed to locally optimize the spectrogram of the current signal, using a chirplet windows dictionary with the computing cost of a single window.

The possibility of generating an optimized spectrogram of the current signal for diagnostic purposes may improve the reliable identification of the trajectories of the fault harmonics by trained personnel, or provide high quality diagnostic data for training neural networks under transient conditions [28, 62, 63], including load oscillations [64], for designing support vector machines for the diagnosis of broken bars in squirrel cage motors [65, 66] or stator short-circuits [67], for implementing deep transfer learning diagnostic systems [13, 68], for building multisource transfer learning networks [69], for managing predictive maintenance strategies bases on machine learning approaches, as in [70], or for implementing other artificial intelligence methods [71, 72] and expert systems [29]. Other application of the LOCS could be the location of informative fre-

6

quency bands for machine performance degradation assessment, as in [73]. Additionally, the optimized spectrogram generated by the LOCS may be needed to distinguish between multiple, simultaneous faults of the IM, as in [74].

This paper is structured in the following way. Section 2 gives a brief presentation of the chirplet transform, and in Section 3 the LOCS is described. In Section 4, it is applied to the diagnosis of two commercial squirrel cage induction motors with different types of faults, a bar breakage and a mixed eccentricity. Section 5 presents the conclusions.

2. The chirplet transform for TF analysis of the machine current

In this section the chirplet transform is described briefly, because it is the foundation of the LOCS.

The detection of fault components under transient conditions, whose frequencies vary with the speed as indicated in Table 1, requires a high resolution spectrogram of the machine current $i(t)$. The process for obtaining it using the STFT consists in multiplying, at each time τ, the current signal by the conjugate of the analysing window $h(t)$, centred at time $t = \tau$, and squaring the modulus of its Fourier transform (FT), as

$$I_{SP}(\tau, \omega) = |I_\tau(\omega)|^2 = \left| \frac{1}{\sqrt{2\pi}} \int e^{-j\omega t} i(t) h(t - \tau)^* dt \right|^2 \qquad (1)$$

Once this process is finished, the analysing window is shifted to the next instant, and the process is repeated. The set of all the spectra obtained at different times is the current spectrogram, which reflects the energy content of the current at each time and frequency.

2.1. The chirplet window

The spectrogram resolution is related to the characteristics of the analysing window $h(t)$ used in (1), which must have a high concentration of energy. The highest energy concentration is achieved by the Gaussian window [34, 75],

$$g(t) = \left(\frac{\alpha}{\pi} \right)^{1/4} e^{\frac{-\alpha}{2} t^2} \qquad (2)$$

7

with a standard deviation $\sigma_t^2 = 1/(2\alpha)$. The FT of the Gaussian window is

$$G(\omega) = \left(\frac{1}{\alpha\pi}\right)^{1/4} e^{-\frac{1}{2\alpha}\omega^2} \tag{3}$$

with a standard deviation $\sigma_\omega^2 = \alpha/2$. The product of the duration σ_t and the bandwidth σ_ω of the Gaussian window gives $\sigma_t\sigma_\omega = 1/2$, the minimum value allowed by the uncertainty principle [76]. Fig. 1 shows the Heisenberg box of the Gaussian window in the TF plane, which is a rectangle with a time width σ_t and a frequency height σ_ω, and a time frequency centre which coincides with the window's.
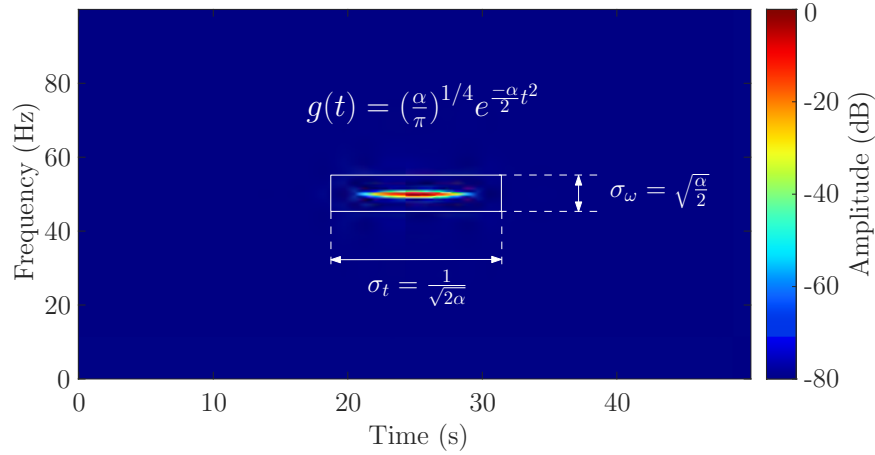

Figure 1: Gaussian window showing its Heisenberg box, which depends on the α parameter of the window.

To optimize the diagnostic spectrogram, the height-to-width ratio of the Gaussian window ($\sigma_\omega/\sigma_t = \alpha$) must be adjusted to match the slope of the fault components [36, 77]. As this can be difficult to achieve in case of fast time-varying conditions, some authors [37, 38, 43, 78] propose the use of a rotated Gaussian window in the TF plane, the chirplet window, by adding a rotation parameter β, as

$$h(t) = g(t)e^{\frac{j\beta}{2}t^2} = \left(\frac{\alpha}{\pi}\right)^{1/4} e^{-\frac{\alpha}{2}t^2} e^{\frac{j\beta}{2}t^2} \tag{4}$$

Fig. 2 shows the chirplet window that is obtained by rotating the Gaussian window of Fig. 1 an angle of $\pi/4$.
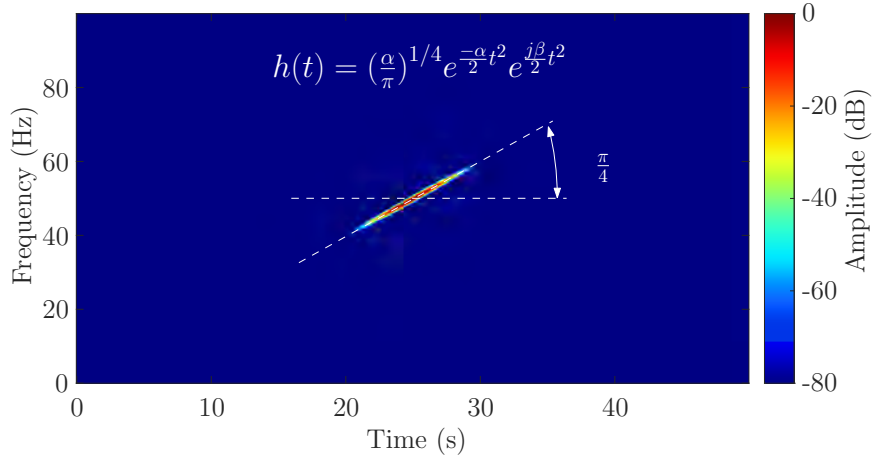
8

Figure 2: Chirplet window, obtained by rotating the Gaussian window of Fig. 1 an angle of $\pi/4$.

Using (1) and (4), the chirplet transform is defined as

$$I_{SP}(\tau, \omega, \alpha, \beta) = \left| \left(\frac{\alpha}{\pi} \right)^{1/4} \frac{1}{\sqrt{2\pi}} \int e^{-j\omega t} i(t) e^{-\frac{\alpha+j\beta}{2}(t-\tau)^2} dt \right|^2 \tag{5}$$

160   *2.2. Optimization of the chirplet window parameters*

The couple of parameters of the chirplet window in (5), α and β, must be adjusted to obtain an optimal overlap between the window and each of the current components, what requires a detailed analysis of the machine characteristics and working conditions, and trained maintenance personnel. An alternative approach consists of obtaining many current spectrograms (5), using a large number of windows with different values of α and β, and selecting for each time and frequency the maximum value among all the spectrograms.

$$\alpha^*, \beta^* = \arg\max_{\alpha, \beta} I_{SP}(\tau, \omega, \alpha, \beta) \tag{6}$$

Due to performance considerations, only a discrete subset of the possible values of α and β can be explored in (6)

$$\alpha^*, \beta^* = \arg\max_{m, n} I_{SP}(\tau, \omega, \alpha_m, \beta_n) \tag{7}$$

9

with $m = 1 \ldots N_\alpha$ and $n = 1 \ldots N_\beta$. Nevertheless, the number of different spectrograms needed to find the optimal values α^* and β^* for each point (τ, ω) of the TF plane is $N_\alpha \times N_\beta$, which can be very high depending on the values of N_α and N_β. This drawback is solved by the proposed LOCS using a single, complex time window.

3. Proposed method for calculating the locally optimized complex chirplet spectrogram (LOCS) of the machine current

The machine current is sampled at a rate f_{samp} during an acquisition time T_S, what generates a total number of current samples $N_{samples} = T_S \times f_{samp}$. Its FFT gives the current spectrum in the frequency band $[0 - f_{samp}/2]$. The sampling frequency f_{samp} can be very high, but only a small fraction of this frequency band is of diagnostic interest, because the main fault harmonic components evolve in a narrow frequency band $[0 - F_S]$ ($F_S \ll f_{samp}$), which depends on the fault type. For the main fault components ($k = 1$ in Table 1), and using industrial supply frequencies, F_S is usually limited to a few hundred Hz [29, 79]. To apply the proposed method, first the harmonic components of the current outside the frequency band of interest are filtered out. In this work, a frequency filter [80] has been used for zeroing the current spectrum outside the diagnostic frequency band.

To obtain the current spectrogram in the diagnostic area (that is, in the rectangular strip of the TF plane of size $T_S \times F_S$ where the fault harmonics show up), a two-step process is developed: first, a suitable dictionary of chirplet windows is built; and, second, all these windows are stored in a single, complex analysing window, which is used to obtain the spectrograms generated by all the windows in the dictionary with a single execution of the STFT algorithm.

3.1. Building of the chirplet dictionary

For building the dictionary (7), first a Gaussian window with the same height-to-width ratio as the diagnostic region is generated. To achieve this,

10

a value of parameter α in (2) equal to $2\pi F_S/T_S$ is used, as

$$g(t) = \left(\frac{\alpha_1}{\pi}\right)^{1/4} e^{\frac{-\alpha_1}{2}t^2}, \quad \text{with} \quad \alpha_1 = \frac{2\pi F_S}{T_S} \tag{8}$$

This Gaussian window is rotated using the parameter β in (4), which is related to the rotation angle φ by [44, 39]

$$\beta(\varphi) = \frac{2\pi F_S}{T_S} \tan(\varphi) = \alpha_1 \tan(\varphi) \quad \varphi \in (-\frac{\pi}{2}, \frac{\pi}{2}) \tag{9}$$

When rotating the Gaussian window, its time width must be reduced to keep its length constant in the joint TF plane, by adjusting the parameter α in (4) as

$$\alpha(\varphi) = \frac{2\pi F_S}{T_S} \frac{1}{\cos(\varphi)} = \frac{\alpha_1}{\cos(\varphi)} \quad \varphi \in (-\frac{\pi}{2}, \frac{\pi}{2}) \tag{10}$$

A discrete set of angular values has been selected to divide the TF region into N_φ sections averagely, as in [44]

$$\varphi_k = -\frac{\pi}{2} + k \cdot \frac{\pi}{N_\varphi + 1} \qquad k = 1, 2, \ldots, N_\varphi \tag{11}$$

Nevertheless, the maximum angle can be reduced from $\pi/2$ in case of numerical instabilities.

Using (11), a dictionary with N_φ chirplet windows is built. The kth ($k = 1, 2, \ldots, N_\varphi$) window is given by

$$h_k(t) = \left(\frac{\alpha_k}{\pi}\right)^{1/4} e^{-\frac{\alpha_k}{2}t^2} e^{\frac{j\beta_k}{2}t^2} \tag{12}$$

where $\alpha_k = \alpha(\varphi_k)$ and $\beta_k = \beta(\varphi_k)$.

190   *3.2. Combining the chirplet windows of the dictionary in a single, complex time window*

The use of a large dictionary of chirplet windows for the analysis of the current signal has an important drawback: a new spectrogram must be build with each dictionary window. Only after all the spectrograms have been obtained
195   it is possible to select the highest value obtained for each time and frequency point. In this section, a single, complex time window is defined in the time domain, which contains all the dictionary windows. In this way, a single execution

11

of the STFT with this novel window generates in parallel all the spectrograms corresponding to the elementary windows of the dictionary.

As only the frequency band $[0\text{-}F_S]$ is of diagnostic interest, data outside this band is normally discarded when using the FFT as signal processing tool. A possible solution to avoid this waste of processing power could be to apply the FFT only to this frequency band. Nevertheless, the number of frequency bins generated by FFT is the same as the number of current samples [81]. Therefore, a reduction of the frequency region results in the reduction of the number of current samples, what may compromise the spectrogram resolution. Another possible solution could be to compute only the spectral bins inside the frequency band of interest $[0\text{-}F_S]$ via the discrete Fourier transform (DFT), which makes use of the full time window. Nevertheless, the computational complexity of the DFT is much higher than the computational complexity of the FFT, what makes this solution inefficient.

The novel solution proposed in this work consists in using the FFT as the signal processing tool for computing the STFT, taking advantage of its speed, and, at the same time, using the full spectral range $[0 - f_{samp}]$ for storing all the windows of the dictionary (11) in a single, complex time window. This solution makes full use of the FFT output, without wasting any computed data. To achieve this goal, the available spectral range of the current spectrum generated by the STFT with a sampling frequency f_{samp}, $[0 - f_{samp}]$, is partitioned into adjacent frequency bands of equal width F_S. Each elementary chirplet window is allocated in one of these frequency bands, by shifting its frequency, as detailed in [61]. Therefore, the number N_φ (11) of elementary chirplet windows that can be allocated is

$$N_\varphi = f_{samp}/F_S \tag{13}$$

To allocate N_φ chirplet windows in consecutive, non-overlapping frequency bands of width F_S, the kth window ($1 \leq k \leq N_\varphi$) is shifted up in the frequency axis, as in [61],

$$h_{\omega_k}(t) = h_k(t) \cdot e^{j\omega_k} = \left[\left(\frac{\alpha_k}{\pi} \right)^{1/4} e^{-\frac{\alpha_k}{2}t^2} e^{\frac{j\beta_k}{2}t^2} \right] \cdot e^{j\omega_k} \tag{14}$$

12

with $\omega_k = (k-1)2\pi F_S$. Finally, the shifted windows are added in the time domain to build the new complex window proposed in this work, as

$$h(t) = \sum_{k=1}^{N_\varphi} h_{\omega_k}(t) \qquad (15)$$

Each elementary chirplet windows contained in the complex time window (15) generates an elementary spectrogram of the current (1). For the kth window, it is given by

$$I_{SP}(\tau, \omega, \alpha_k, \beta_k) = \left| \left(\frac{\alpha_k}{\pi} \right)^{1/4} \frac{1}{\sqrt{2\pi}} \int e^{-j(\omega+\omega_k)t} \cdot i(t) \cdot h_k(t-\tau)^* dt \right|^2 \qquad (16)$$

In this way, the spectrogram generated by the kth chirplet windows is also shifted in the frequency axis by ω_k. A single execution of the STFT using (15) as the analysing window generates, in parallel, as many different elementary spectrograms (5) as elementary windows are contained in (15), allocated in non-overlapping frequency bands. The maximum values obtained at each point of the TF plane among these spectrograms are selected in the final result, according to (7).

3.3. Summary of the proposed methodology

The proposed methodology for obtaining the LOCS of a current signal can be summarized in the following points:

1. The current signal is acquired during a time T_S with a sampling frequency rate of f_{samp}.

2. The width of the frequency band with diagnostic interest is selected as F_S ($F_S << f_{samp}$). This defines a Gaussian window with the same height-to-width ratio than the diagnostic region F_S/T_S, (8), the number of rotated versions of this base window (13) and their shapes in the TF plane (14). The content of the current signal outside this frequency band is filtered out.

3. A single complex time window is built by displacing each rotated window to a unique frequency band and adding all of them (15). This window

13

is able to display optimally all the possible harmonic components in the selected TF region.

4. The STFT of the current signal is calculated using this complex time window in the usual way (5): for each time instant, the window is shifted to that time, multiplied by the current signal, and the result is processed using the FFT. This process is repeated for each current sample, and generates a single spectrogram, which contains all the spectrograms corresponding to the elementary chirplet windows, allocated in different, non-overlapping frequency bands.

5. All the elementary spectrograms are combined to produce a final result by selecting for each point in the TF region the maximum value obtained for that point (7).

3.4. Practical example with a synthetic current signal

To better illustrate the proposed methodology, the LOCS is calculated for a synthetic current signal $i(t)$ (Fig. 3), which contains three components: a 60 Hz sine wave, and two linear chirps with a frequency slope of ± 1 Hz/s, with an initial frequency of 60 Hz. The simulation time is 30 s, with a time step of 1/360 s, as

$$i(t) = \cos(2\pi 60 t) + 0.05 \cos(2\pi(60 t \pm 0.5 \cdot t^2)) \tag{17}$$

The bandwidth of the region with diagnostic interest has been chosen to be F_S=120 Hz, higher than the maximum frequency expected for the current components. The Gaussian window with the same height-to-width ratio as this region has a parameter $\alpha_1 = 2\pi 120/30$ (8). As the signal has been generated at a rate of $f_{samp} = 360$ Hz and the diagnostic bandwidth is $F_S = 120$ Hz, three elementary chirplet windows can be allocated in the [0 - 360] Hz spectral range generated with the STFT, applying (13) $f_{samp}/F_S = 360/120 = 3$. The proposed complex time window, defined by (15), is built by combining three copies of this elemental window, rotated $[-\pi/8, 0, \pi/8]$ respectively, as given by (11). This complex window is depicted in the time domain in Fig. 4, showing
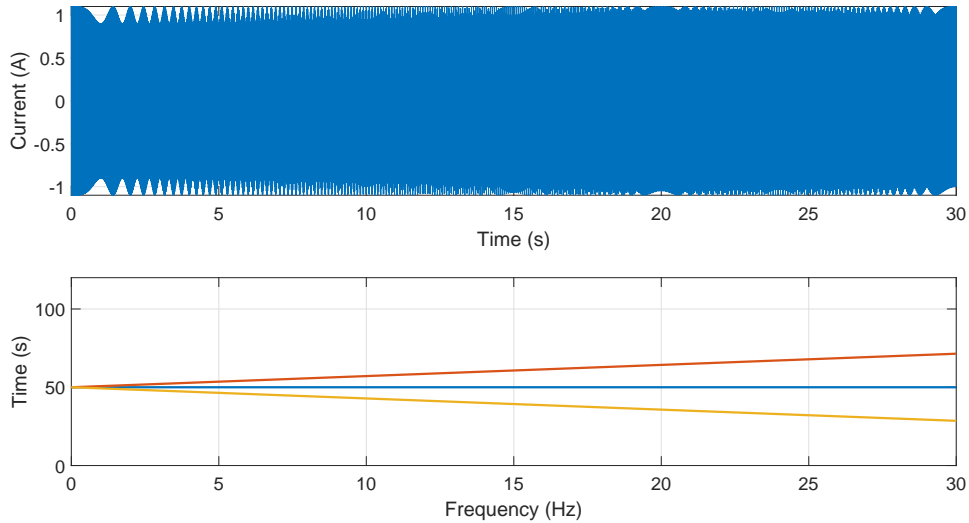
14

Figure 3: Synthetic current signal (17) (top) and frequency of its chirp components (bottom).

both its real (top) and its imaginary part (top). Its three elementary chirplet
windows are allocated in three consecutive, non-overlapping frequency bands,
and their amplitudes in the frequency domain are represented in Fig. 4, bottom.
Its spectrogram, shown in Fig. 5, left, displays these three elementary chirplet
windows in adjacent, non-overlapping bands of the TF plane, showing their
different orientations.

A single STFT of the synthetic current signal (17), using the single, complex
time window shown in Fig. 4, generates in parallel three elementary spectro-
grams, located in three different frequency bands, as seen in Fig. 5, right.

Each elementary chirplet windows highlights the harmonic component with
its same slope. The pure Gaussian window has a maximum overlap with the
fixed-frequency component of the current, and the two chirplet windows have
maximum overlap with the chirp components of the current. Their combination,
following the rule (7), generates a high resolution current spectrogram, shown
in Fig. 6. As the three elementary spectrograms are generated in parallel, the
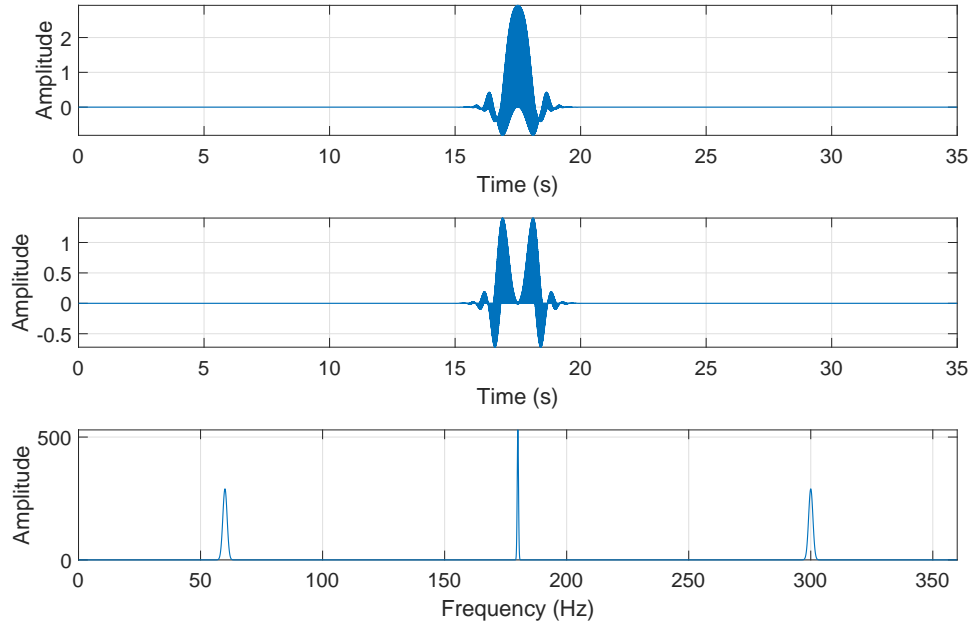computational cost is that of a single execution of the STFT.

15

Figure 4: Real part (top) and imaginary part (middle) of the complex time window used to analyse the synthetic current signal. This window contains 3 elementary chirplet windows, with rotation angles $[-\pi/8, 0, \pi/8]$, allocated in three consecutive, non-overlapping frequency bands, whose amplitudes in the frequency domain are represented in the bottom plot.

4. Experimental validation

The LOCS is applied in this section to asses the condition of two different commercial motors, with two different faults, one with a bar breakage and the other one with mixed eccentricity.

4.1. Application of the LOCS to detect a bar breakage

For this experimental test, the IM of Appendix A has been used. Bar breakages can be produced by the high mechanical and thermal stresses that the rotor cage supports, especially during the startup process, due to the high currents flowing through the cage. These high currents produce small deformations in the bars and end-rings that, combined with the expansions and contractions caused by the thermal processes, and with the unavoidable manufacturing process, produce small cracks in the junction that may led to the complete breaking
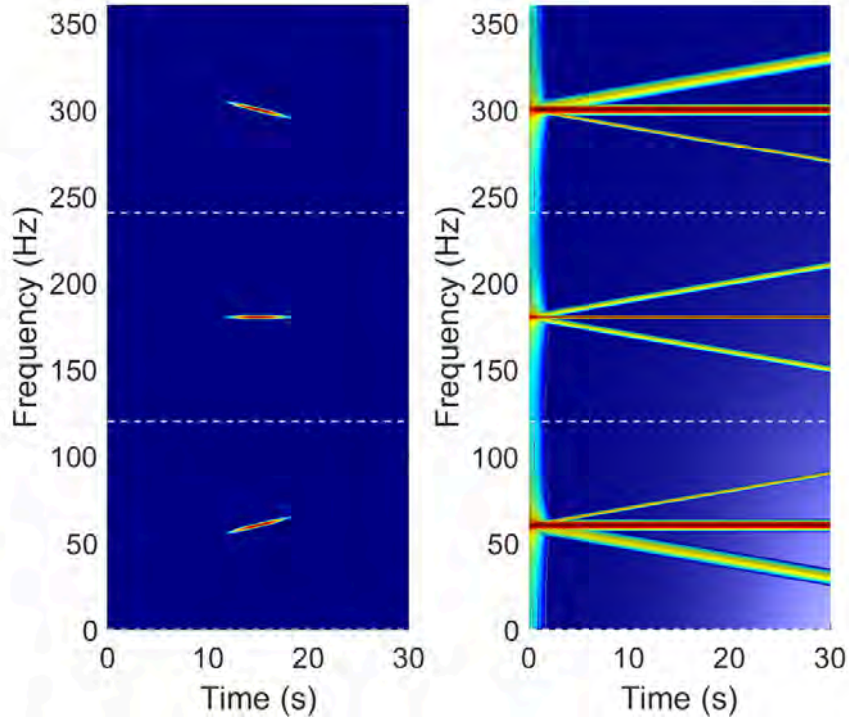
16

Figure 5: Current spectrogram of the synthetic signal (17) (right), generated with a single execution of the STFT algorithm with the proposed complex time window (left). Each elementary chirplet window generates in parallel a current spectrogram that highlights the harmonic component with its same slope.

of the bars in this region of maximum stresses [82, 83]. To better reproduce this type of fault, a hole has been drilled in one bar at this junction, as in [84]. Fig. 7 shows a faulty and a healthy rotor cage (left), and a close view of the provoked fault (right).

Fig. 8 shows the test-bench used in this work, and Fig. 9 shows the schema of the experimental setup. In this test-bench, two identical induction motors are mechanically coupled. One of them is the motor under test, with a broken bar provoked fault, and the other one is fed from a variable speed drive (VSD), and works in generator regime. By adjusting the VSD output frequency it is possible then to adjust the load level of the IM under test. As shown in Fig. 9, one of
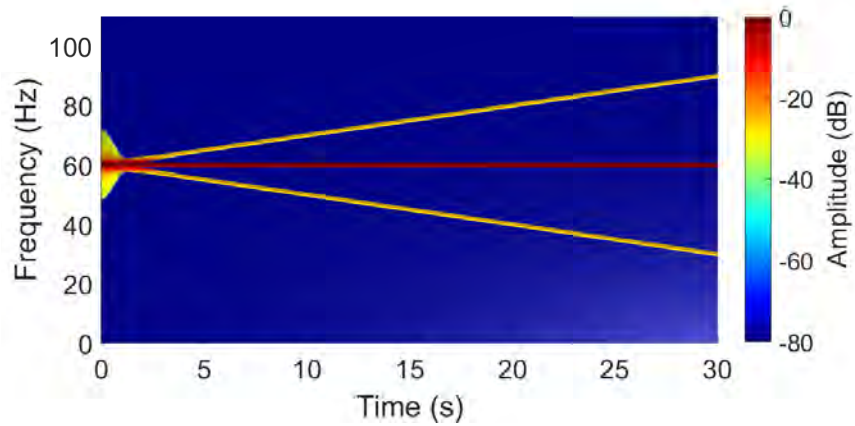
17

Figure 6: Spectrogram of the current signal (17), obtained by combining the three spectrograms of Fig. 5, right, according to (7). It shows with a high resolution the sinusoidal and chirp components of the current.

Figure 7: Experimental motor of Appendix A with a provoked broken bar. Comparison with a healthy rotor (right) and close view of the bar breakage, at the junction with the end ring (right).

the stator currents of the motor under test has been measured with a Chauvin Arnoux MN60 current clamp (nominal measuring scope: 100 mA–20A, ratio input/output: 1 A/100 mV, intrinsic error: $\leq 2\% + 50$ mV, frequency use: 400 Hz–10 kHz), the speed with a 200 pulse/revolution encoder, and all the data has been collected using a Yokogawa DL750 oscilloscope, as depicted in Fig. 9. The acquired data is transferred through an Ethernet link to the personal computer

18

(CPU: Intel Core i7-2600K CPU @ 3.40 GHZ RAM memory: 16 GB), where it is processed using Matlab (Version: 9.10.0.1602886 R2021a) to produce the results and images shown in this work.
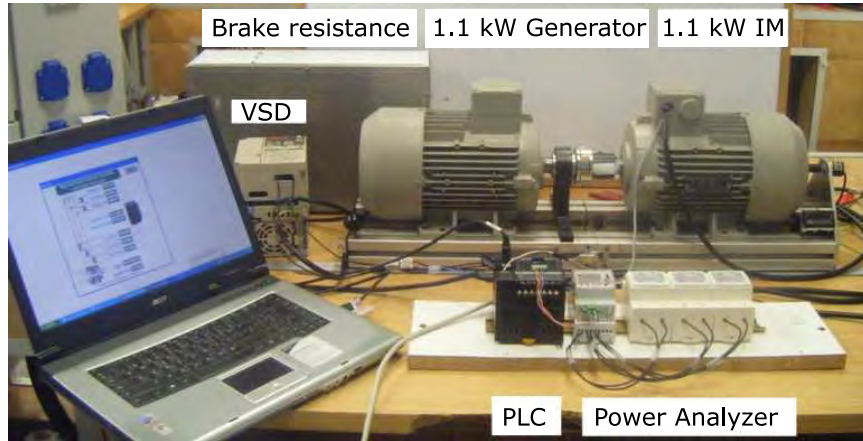

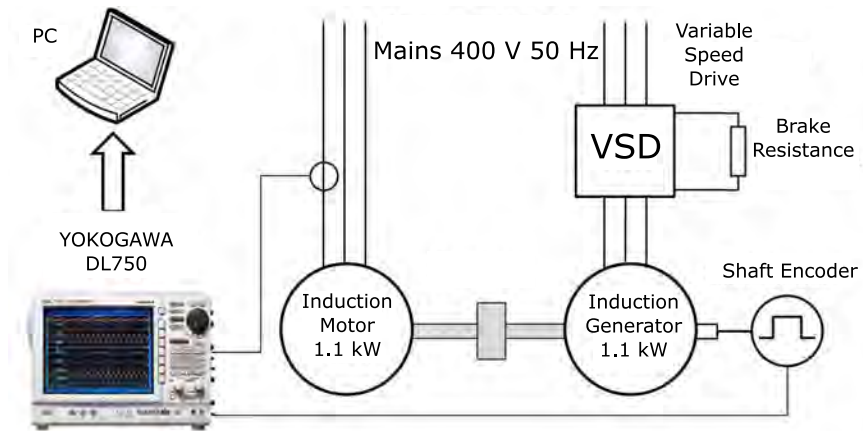Figure 8: Condition monitoring test-bench used in this work.

Figure 9: Schema of the condition monitoring test-bench used in this work.

The stator current, shown in Fig. 10, has been acquired during a start-up transient (10 seconds), at a frequency rate $f_{samp} = 5000$ Hz. It is worth mentioning that it has multiple components due to noise and to the non-ideal characteristics of the motor, as can be observed in the enlarged view of Fig. 10,
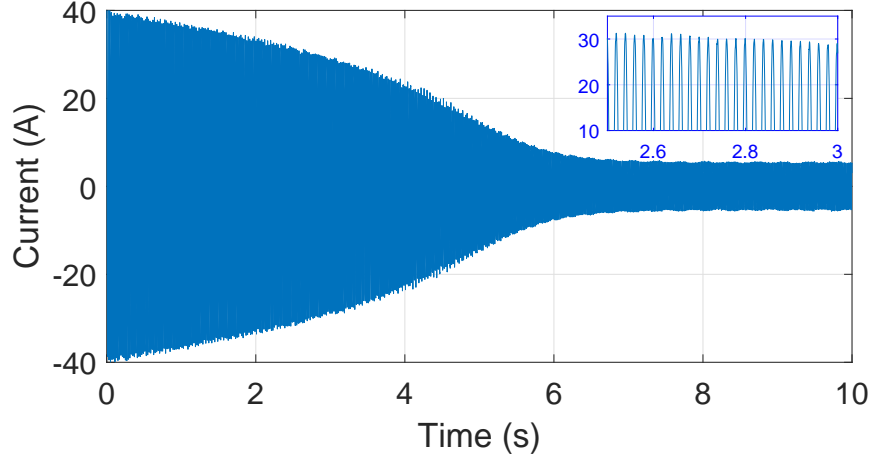
19

top.

Figure 10: Current of the motor of Appendix A with a broken bar, during the start-up transient. This signal has multiple components caused by noise and non-ideal characteristics of the motor, as can be observed in the enlarged view.

The main fault harmonics generated by a bar breakage ($k = 1$ in Table 1) have a frequency that is given by

$$f_{bb} = f_1(1 \pm 2s) \tag{18}$$

In particular, the main fault harmonic that has a frequency

$$f_{LSH} = f_1 \cdot (1 - 2s) \tag{19}$$

is commonly used for the diagnosis of broken bars, and is denoted as the lower side-band harmonic (LSH). According to (19), during a start-up transient the LSH generates a typical V-shaped fault signature [14, 36], shown in Fig. 11. The ability to display this fault signature in the spectrogram of the experimental current signal constitutes a validation of the LOCS.

The frequency band of diagnostic interest has been chosen to be [0 - 125 Hz], where the LSH given by (19) is expected to show up, for $f_1 = 50$ Hz. The number of chirplet windows that can be stored in the single, complex time window with a sampling frequency of 5 kHz is $N_\varphi = 5000/125 = 40$ (13). The
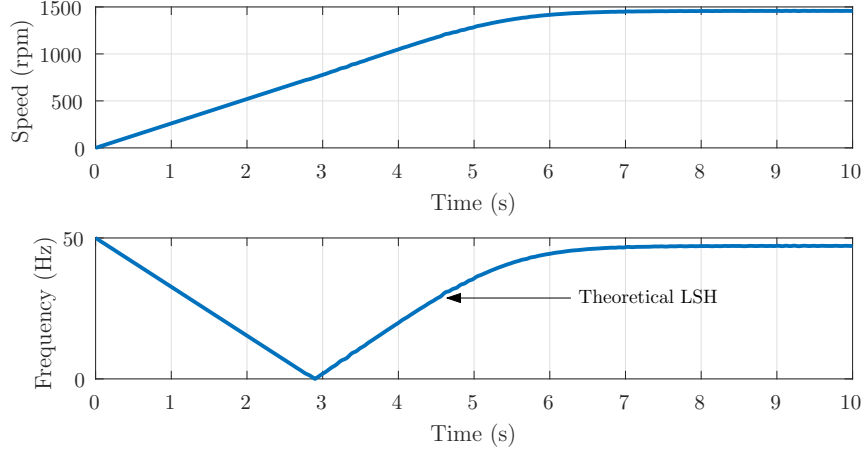
20

Figure 11: Measured speed during the start-up of the motor of Appendix A (top), with a broken bar, and theoretical evolution of the LSH fault harmonic, according to (19). The ability to display this fault signature in the spectrogram of the experimental current signal constitutes a validation of the method proposed in this work.

rotation angles of these windows are (11)

$$\varphi_k = -\frac{\pi}{2} + k \cdot \frac{\pi}{41} \qquad k = 1, 2, \ldots, 40 \tag{20}$$

The parameters α and β of these chirplet windows are obtained from (20), using (9) and (10). The resulting complex time window (15) is shown in Fig. 12, which depicts its real (top) and imaginary part (middle). It contains 40 elementary chirplet windows, allocated in 40 contiguous 125 Hz bands, whose amplitudes in the frequency domain are represented in Fig. 12, bottom.

Fig. 13 depicts the spectrogram of the current of Fig. 10, obtained using this complex analysing window. A single run of the STFT algorithm (5) generates 40 elementary spectrograms, in adjacent frequency bands, as shown in Fig. 13, right. Each elementary spectrogram is located in the same frequency band as its chirplet window (Fig. 13, left). Fig. 14 shows an enlarged view of two of these frequency bands. As the components of the complex window have different rotation angles, each elementary spectrogram highlights the current component with the same slope as the corresponding chirplet window. As the
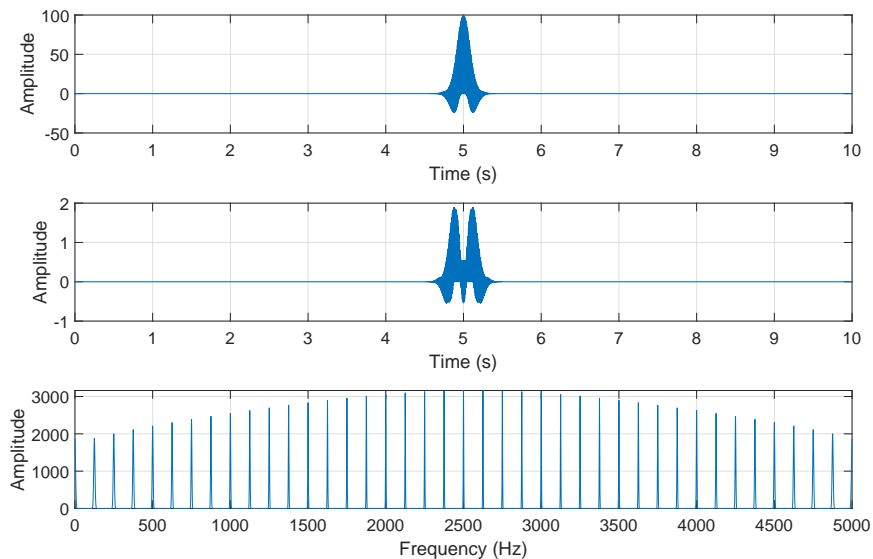
21

Figure 12: Complex time window used to generate the current spectrogram, real (top) and imaginary part (middle). It contains 40 elementary chirplet windows, allocated in 40 contiguous 125 Hz bands, whose amplitudes in the frequency domain are represented in the bottom plot.

chirplet windows dictionary has been designed to divide the TF diagnostic region into 40 sections averagely (20), it is flexible enough to capture a wide range of harmonic components, independently of their slope or their time position, without any additional adjustment. It has to be noted that, to avoid the strong leakage of the fundamental, this component has been extracted as in [85, 86] (using a digital filter), and processed separately.

All the elementary spectrograms shown in Fig. 13, right, are combined using the rule (7), what generates a high resolution current spectrogram, depicted in Fig. 15. It shows clearly the ridges of both the fundamental and the LSH components. Second-order components generated by the fault are also displayed, which helps get a more reliable diagnostic. Fig. 16 shows a 3D view of Fig. 15, to better display the TF trajectories of the current components.

For comparison purposes, the current spectrogram has also been obtained using a single Gaussian window, with a parameter α given by (8), without any
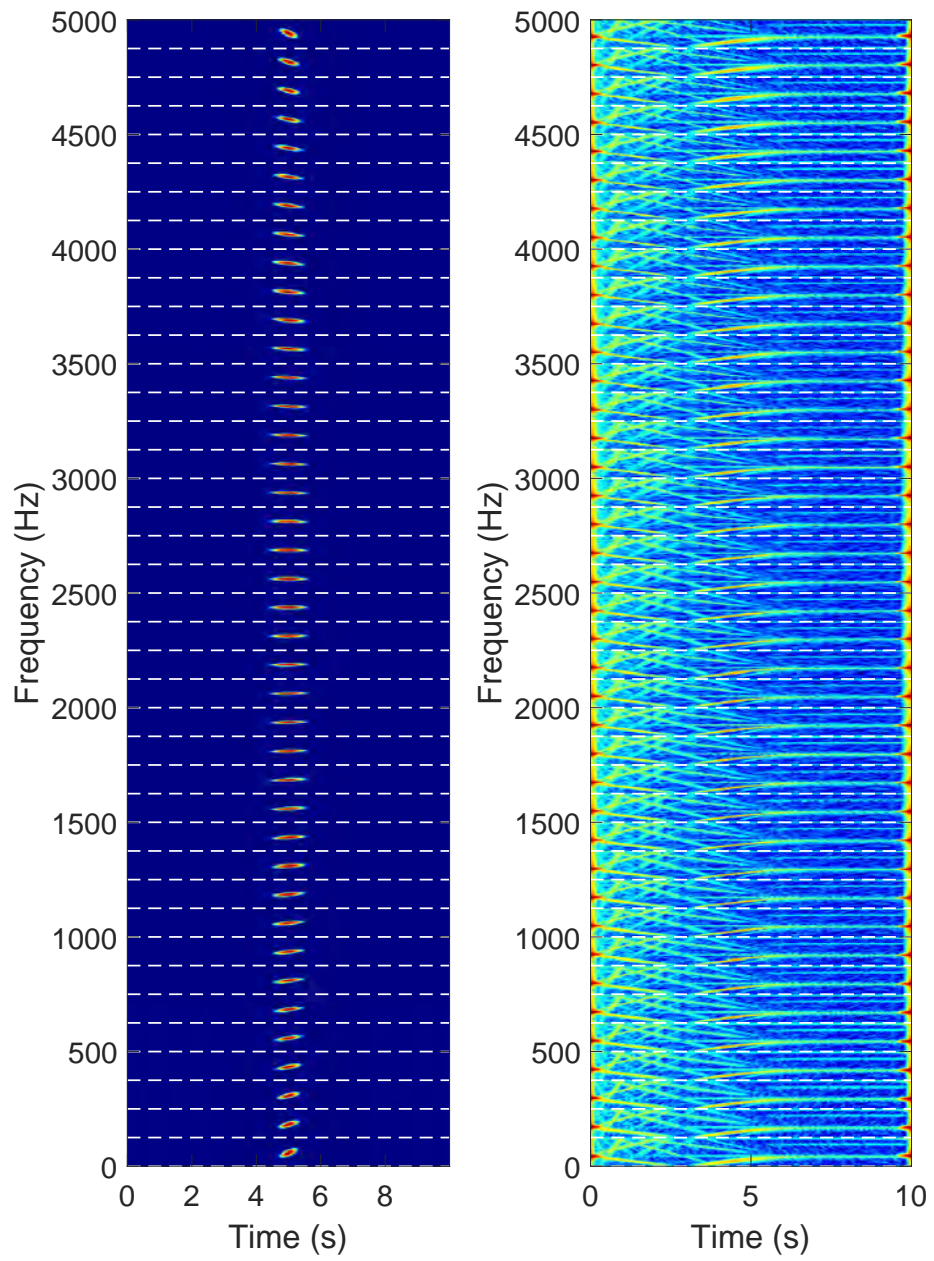
22

Figure 13: Current spectrogram of the faulty motor of Appendix A during the start-up transient (right). It shows the 40 elementary spectrograms obtained in parallel, using the single, complex time window of Fig. 12 (left).
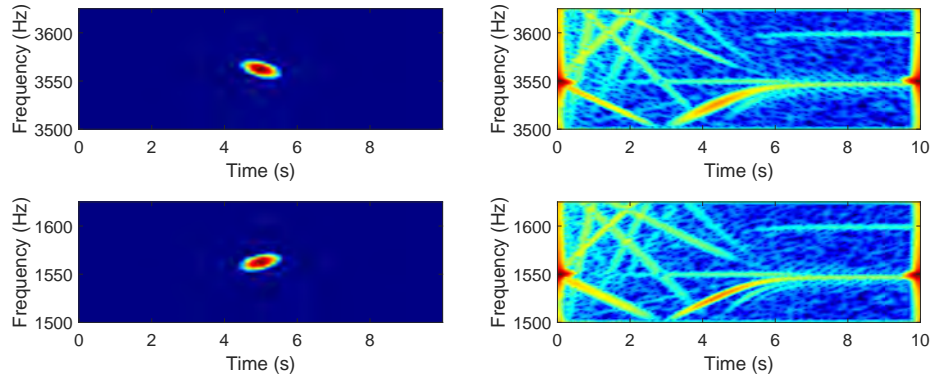
Figure 14: Enlarged view of two different frequency bands of the spectrogram shown in Fig. 13, corresponding to elementary chirplet windows of slopes with different sign (left). The portions of the spectrogram generated by these different elementary windows (right) highlight the harmonic components with similar slopes in the TF plane.
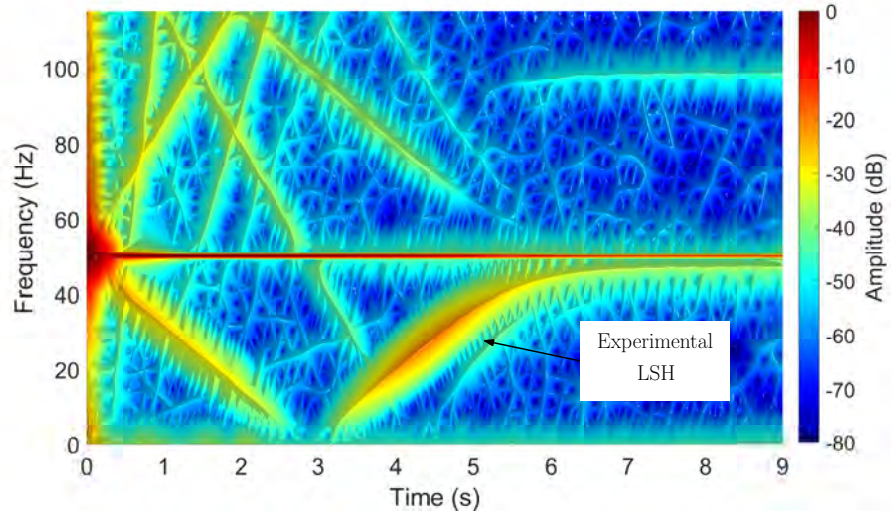

Figure 15: High resolution current spectrogram of the motor of Appendix A obtained with the LOCS using the complex window of Fig. 12. The time needed to build it has been 12.68 seconds.

rotation, and it is shown in Fig. 17. The spectrogram obtained with the proposed complex window (Fig. 15) improves clearly the visibility of the components ridges compared with Fig. 17, without increasing the computational cost. It
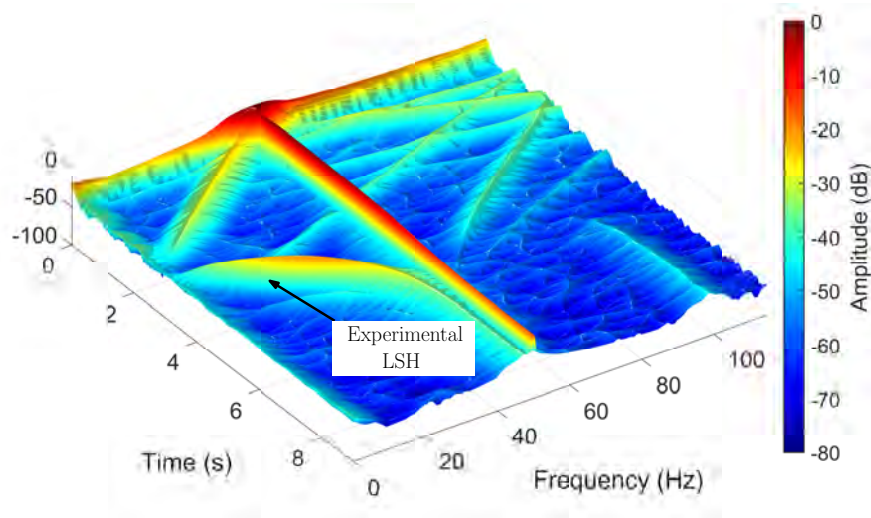
340

24

Figure 16: 3D view of the high resolution spectrogram displayed in Fig. 15, showing the TF trajectories of the current components.

takes 12.68 seconds to obtain Fig. 15, and 12.43 seconds to obtain Fig. 17, practically the same.

One of the possible applications of the LOCS is the extraction of relevant features in order to train and apply expert systems, such as deep learning neural networks or support vector machines. To this end, the spectrogram displayed in Fig. 15 has been processed with the harmonic order tracking approach (HOTA) described in [87], which reduces the 2D spectrogram of Fig. 15 to 1D plot that displays the amplitudes of the harmonic components in the harmonic order domain of the broken bar fault (Fig. 18, top). As only the harmonic components with an integer harmonic order are generated by the broken bar fault, the small set of the eight amplitudes corresponding to the fault harmonics up to the fourth order, plus the fundamental one (Fig. 18, bottom), extracts the relevant information contained in the full spectrogram, and can be used as the input features of automatic expert systems for fault diagnosis. Additional harmonics with non-integer harmonic index have been displayed in Fig. 18, bottom, to facilitate the assessment of the fault.
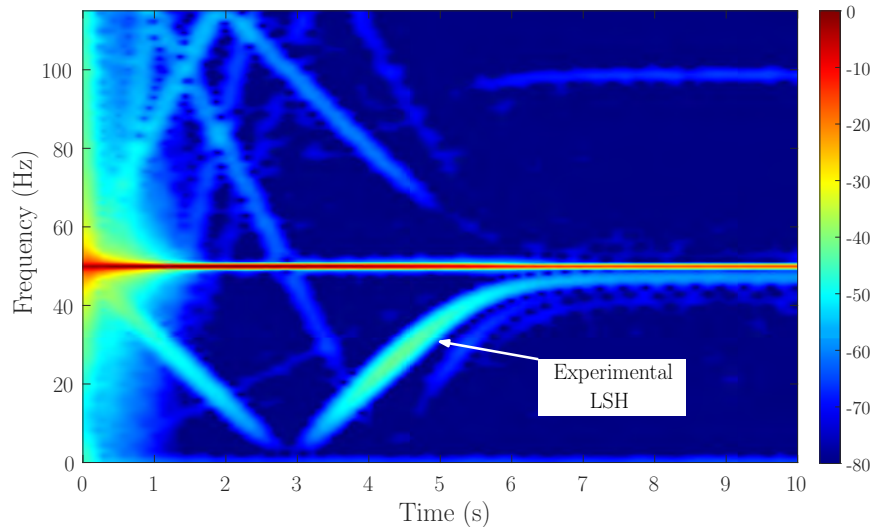
25

Figure 17: Traditional spectrogram of the analysed TF region, obtained using a single, non-rotated Gaussian window with the same height-to-width ratio as the diagnostic region. The ridges of the fault components are not clearly defined in this spectrogram, although the time needed to build it has been 12.43 s, practically the same as the LOCS.

4.2. Application of the LOCS to detect a mixed eccentricity fault

For this experimental test, the IM of Appendix B has been used, with a mixed eccentricity that has been provoked using eccentric rings as in [88, 89]. A motor whose characteristics are given in Appendix B has been endowed with an artificially provoked mixed eccentricity fault, by replacing the original bearing of the motor (see Fig.19.a) a new one (Fig. 19.d) with a smaller outer diameter and a greater inner diameter. Besides, two precision eccentric machined steel rings (Fig. 19.b and Fig. 19.c) have been used for adjusting the new bearing to the bearing housing (Fig. 19.b) and to the shaft (Fig. 19.c). The cylindrical surfaces of both rings are eccentric, 0.4 mm in the case of the outer ring b, and 0.4 mm in the case of the inner ring c. Fig. 19.e shows the new assembly mounted on the shaft, obtaining in this way a rotor with a 30% of static eccentricity and a 30% of dynamic eccentricity.

The measurement equipment used for this test is the same one used in Section 4.1. The stator current has been acquired during a start-up transient (10
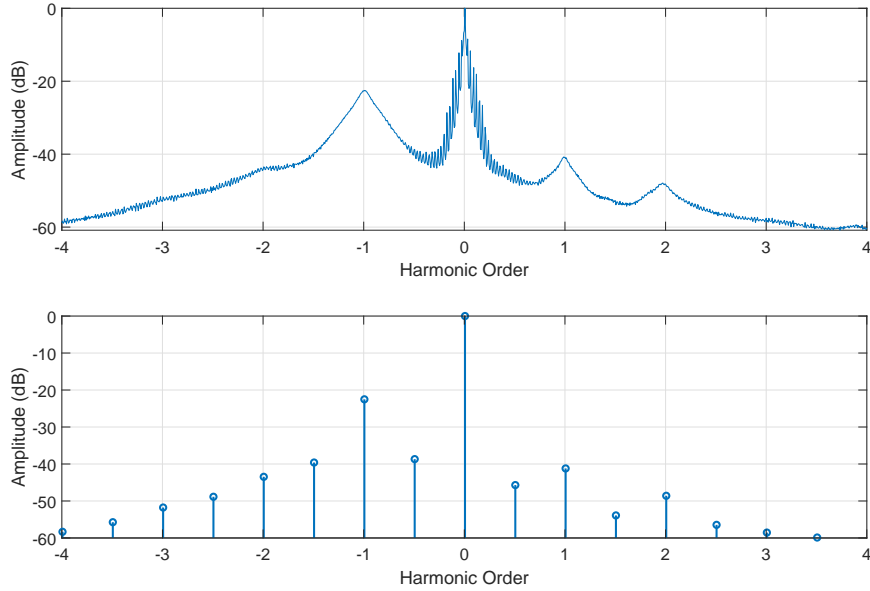
26

Figure 18: Amplitude of the harmonic components in the spectrogram generated by the LOCS (Fig. 15), represented in the harmonic order domain of the broken bar fault (top). The eight amplitudes of the harmonics with integer harmonic index up to the fourth order, the only ones generated by the broken bar fault, plus the fundamental component, have been extracted (bottom). Additional harmonics with non-integer harmonic order have been displayed to facilitate the assessment of the fault.

seconds), at a frequency rate $f_{samp} = 5000$ Hz.

The frequencies of the main fault harmonic produced by a mixed eccentricity fault are ($k = 1$, $p = 2$ in Table 1)

$$f_{ecc} = f_1 \cdot (1 \pm \frac{1 - s}{2}) \tag{21}$$

According to (21), a mixed eccentricity fault generates during the start-up of a line fed IM (50 Hz) two main signatures, one increasing from 50 Hz towards 75 Hz and other decreasing from 50 Hz towards 25 Hz. Both of them become horizontal components parallel to the supply frequency component at steady state. Again, the ability to display this fault signature in the current spectrogram constitutes a validation of the LOCS.

The frequency band of diagnostic interest has been chosen to be [0 - 125 Hz],
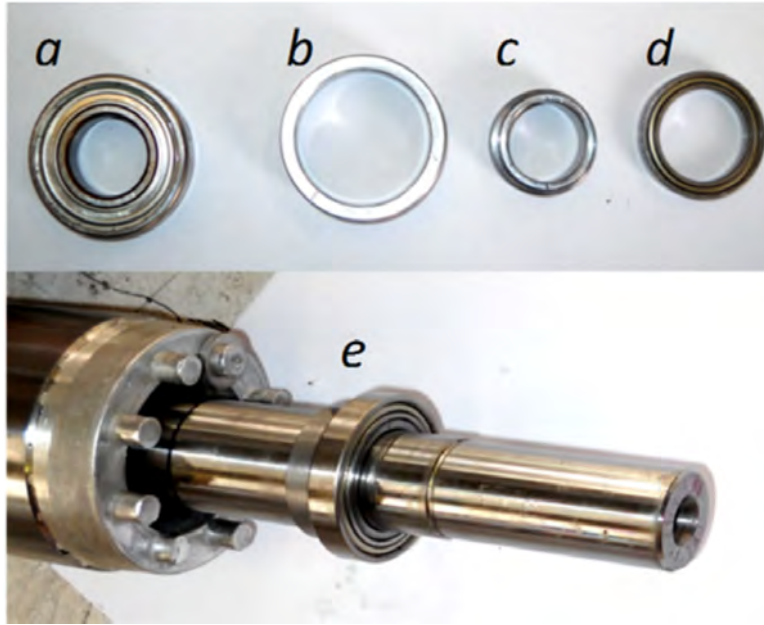
27

Figure 19: Rotor of the eccentric motor unit. Top, from left to right: a) original bearing, b) external and c) internal eccentric rings, and d) new bearing. Bottom: e) mounted unit on the shaft.

where the mixed eccentricity fault harmonics with a frequency given by (21) are expected to show up, for $f_1 = 50$ Hz. As the dimensions of the diagnostic TF strip are the same as in Section 4.1, the complex window of Fig. 12 has been reused to detect the eccentricity fault.

385   The current spectrogram obtained with the complex window of Fig. 12, depicted in Fig. 20, shows with a high resolution the ridges of the fundamental and the eccentricity related components. Moreover, second-order fault components can also be observed in this spectrogram, which helps get a more reliable diagnostic. Fig. 21 shows a 3D view of Fig. 20, to better display the TF trajectories

390   of the current components.

It is worth mentioning that the V-shaped characteristic signature of an incipient rotor asymmetry can be also observed in this spectrogram, with a much lower level than the one detected in the spectrogram of Fig. 15 (-35 dB instead
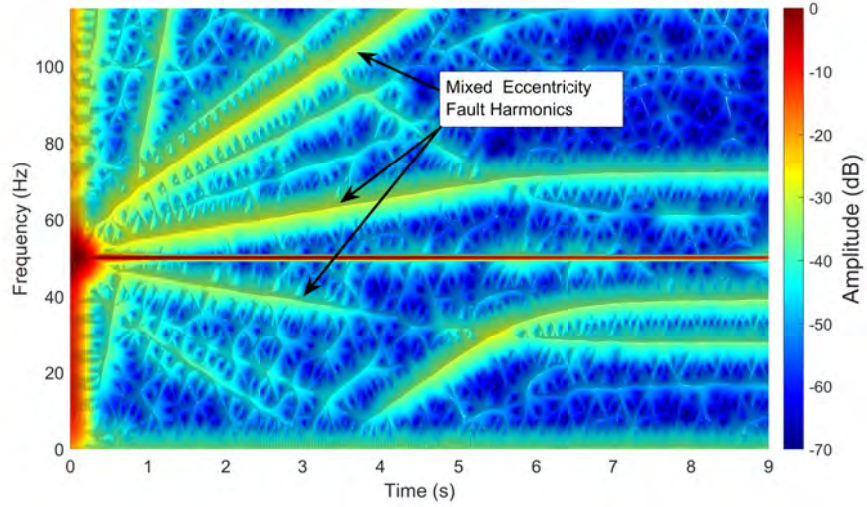
Figure 20: High resolution current spectrogram of the eccentric motor of Appendix B obtained with the LOCS using the complex window of Fig. 12.
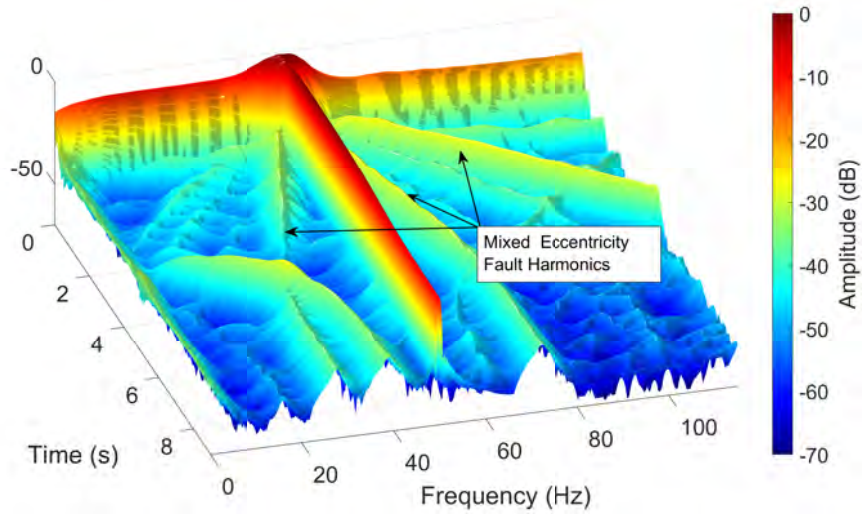

Figure 21: 3D view of the high resolution spectrogram displayed in Fig. 20, showing the TF trajectories of the current components.

of -20 dB). This fact is common in industrial machines, due to imperfections

395 in the process of cage manufacturing, and the capability of LOCS to detect it

29

shows that it can be applied also to the detection of incipient damages, such as partial broken rotor bars.

The remarkable capability of the proposed approach to correctly display fault harmonics with different slopes, generated by different, simultaneous types of faults, under different types of transients, using a single time window, is due to the novel design of the LOCS. This is precisely one of the strengths of the diagnosis of IMs using transient stator currents [58], obtained over a wide range of rotor slip values: the ability to display the unique trajectories of the fault harmonics in the TF plane. This enables their reliable identification even in case of simultaneous faults, in spite of the presence of intersection points where these harmonics have the same instantaneous frequency. On the contrary, the analysis of permanent stator currents assumes a single value of the slip, which may lead to misdiagnosis if different harmonic components have the same frequency for that slip value, as for example in the case of slow varying loads with the same frequency as the bar breakage fault harmonics [90].

It is also remarkable that the same complex window of Fig. 12 has been used to detect different types of faults with different motors. This is due to the flexibility of the proposed approach, which is able to identify many different current components within a given TF area, thanks to the high number of different chirplet windows that are included in the proposed complex analysing window.

It must be mentioned that the proposed approach may be difficult to apply to the analysis of very short transients, as the start-up of unloaded low-power IMs driving very low inertia loads [91]. In this case, the electromagnetic transient and the border effects of the STFT at the beginning of the start-up transient may blur the fault harmonics during a great part or this transient, if it is very short. This limitation is common to all linear time-frequency transforms. Nevertheless, due to the flexibility of the LOCS, the fault harmonics are also clearly displayed in stationary regime, as seen in Fig. 15 and Fig. 20. Besides, the combination of elementary chirplets with a wide parameters range help reduce the border effect, as can be seen by a direct comparison of this effect in Fig. 15, with the

30

LOCS, and in Fig. 17, which uses a single type of analysing window.

4.3. Comparison with related works

To further assess the validity of the proposed approach, it is compared in this section with other methods proposed in the technical literature for the IM diagnosis based on the analysis of the transient stator current, the single-window chirplet transform used in [46], the multi-window Gabor transform used in [61], and the wavelet transform used in [34], the CCWT. These transforms have been applied to generate the spectrogram of the current signal of the IM of Appendix A with a broken bar fault, shown in Fig. 11, and their results will be compared with the spectrogram generated with the proposed approach, shown in Fig. 15.

Fig. 22 shows the spectrogram of the start-up stator current of the motor of Appendix A with a broken bar, obtained with the chirplet transform proposed in [46] using a single chirplet window. The time needed to build it has been 12.74 seconds, practically identical to the LOCS. This spectrogram shows with a high resolution the ascending part of the LSH, whose slope in the TF plane matches the slope of the chirplet window used for the analysis. Nevertheless, all the other harmonic components of the current appear blurred, because their slope do not match the orientation of the chirplet window. To achieve the same result than the LOCS, this method should be applied 40 times, each one with a different chirplet orientation, and the maximum value obtained for each point of the TF should be selected for the final spectrogram. This would increase the time needed with this approach up to more than 500 seconds, that is, over 40 times the time needed by the LOCS.

Fig. 23 shows the spectrogram of the start-up stator current of the motor Appendix A with a broken bar, obtained with the multi-band Gabor transform proposed in [61] using multiple Gaussian windows stored in different bands of a single complex time window. The time needed to build it has been 13.35 seconds, practically identical to the LOCS. Nevertheless, due to the fixed orientation of the Gaussian windows used in [61] (only the aspect ratio of this type of window can be adjusted), the trajectories of the fault harmonics in Fig. 23 lack the
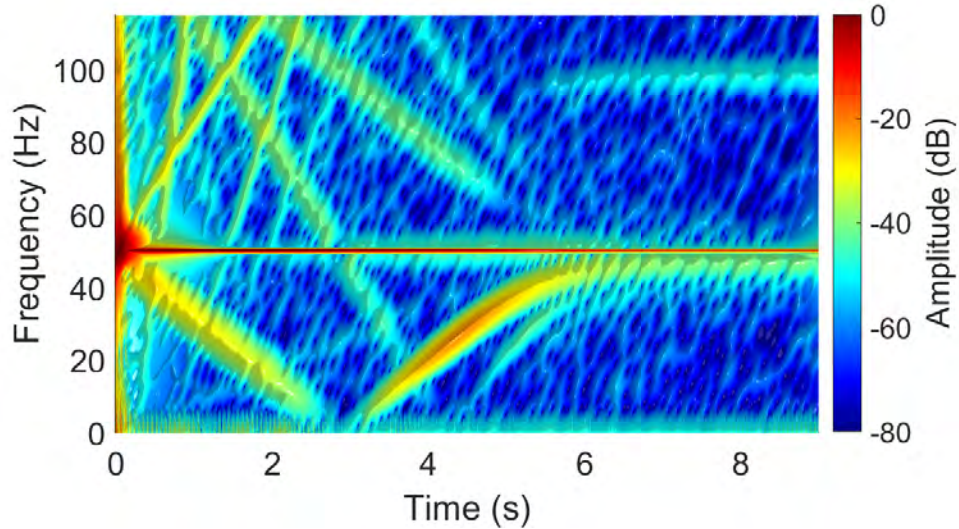
Figure 22: Spectrogram of the current of the motor of Appendix A with a broken bar obtained with the chirplet transform proposed in [46] using a single chirplet window. The time needed to build it has been 12.74 seconds.

resolution obtained in Fig. 15, where the added degree of freedom of the chirplet, its orientation, allows for a better matching between the analysing windows and the slopes of the harmonic components of the current.

460   Fig. 24 shows the scalogram of the start-up stator current of the motor Appendix A with a broken bar, obtained with the CCWT proposed in [34]. This scalogram, which has been generated using the 'Wavelet Analyzer' toolbox available in Matlab, displays the modulus of the complex coefficients obtained when applying the CCWT using as analysing mother wavelet the derivative of

465   a Gaussian (DOG) of order 8, with 400 scales. The scalogram displays correctly the LSH, but fails to display any other current harmonics components, except the fundamental one.

5. Conclusions

A novel technique for obtaining a locally optimized chirplet current spec-
470   trogram, the LOCS, has been proposed and tested in this work. It consists of
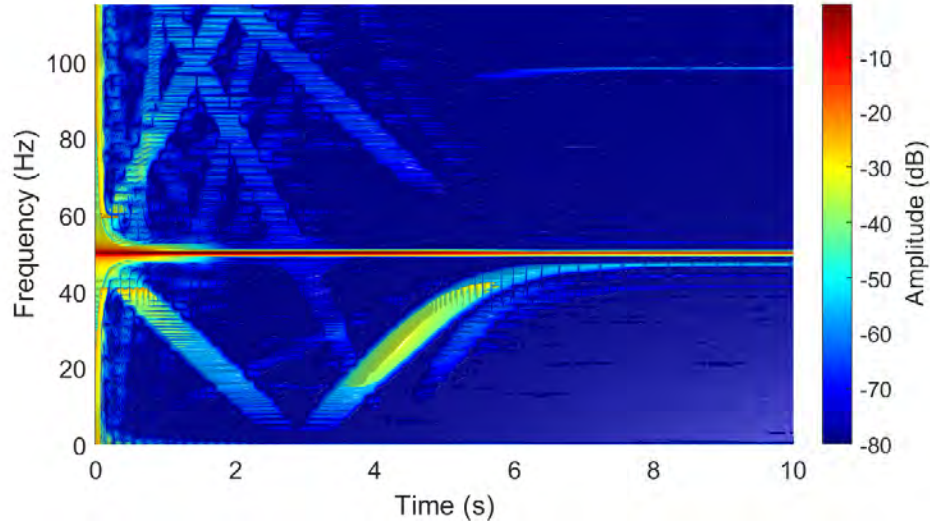
32

Figure 23: Spectrogram of the current of the motor of Appendix A with a broken bar, obtained with the multi-band Gabor transform proposed in [61], using multiple Gaussian windows stored in different bands of a single complex time window. The time needed to build it has been 13.35 seconds.

a two-step process: first, a suitable dictionary of chirplet windows is built, by rotating a base Gaussian window to divide the TF plane averagely; and, second, all these dictionary windows are stored in a single complex window in the time domain, using non-overlapping, adjacent frequency bands. A single STFT with this novel complex time window generates in parallel the spectrograms corresponding to all the elementary chirplet windows, allocated in separated spectral bands, what avoids the need of applying the STFT to each chirplet window in the dictionary and reduces the computational cost. The locally optimized value of the current spectrogram is obtained as the maximum value among all the elementary spectrograms for each time and frequency points. Moreover, once designed, this complex time window can be reused for the analysis of the diagnostic region with different machines or with other types of faults. The LOCS has been tested in this work with a motor with a bar breakage and another with mixed eccentricity. Compared with equivalent works, which built a different

33
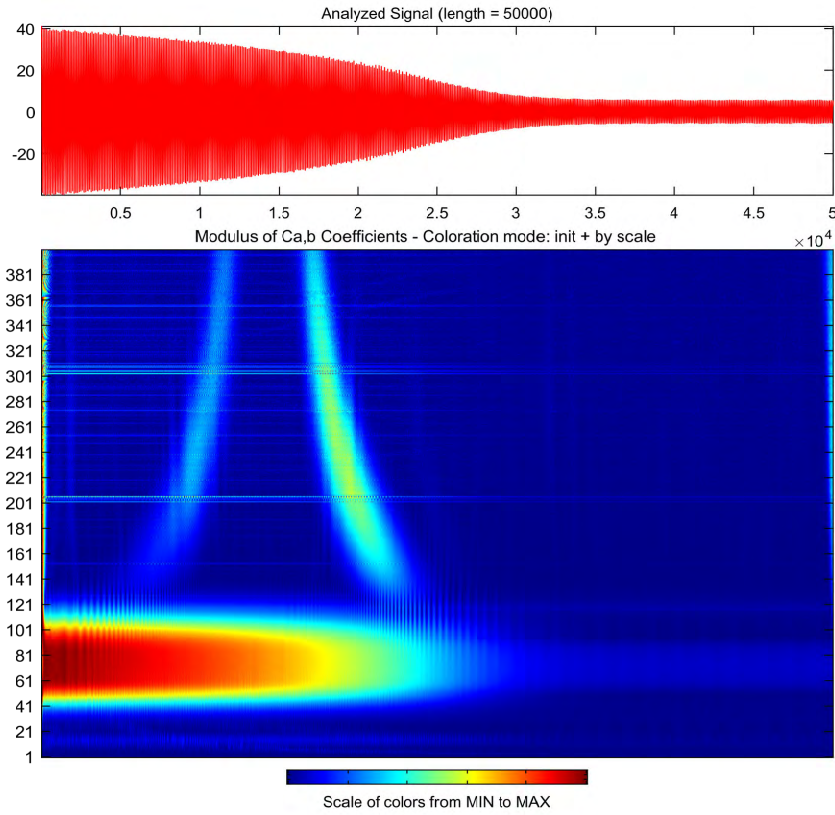
Figure 24: Scalogram of the current of the motor of Appendix A with a broken bar, representing the modulus of the complex coefficients obtained when applying the CCWT with a DOG analyzing mother wavelet of level 8, and 400 scales. The scalogram displays the LSH, but fails to display any other current harmonics components, except the fundamental one.

spectrogram for each window from a dictionary, the proposed LOCS generates the same high-resolution spectrogram in a fraction of 1/40 of the total time, in the case of the motors analysed in this work.

The application of LOCS to the diagnosis of other types of faults, such as interturn short circuits, is currently being developed. Another line of research is the use of LOCS for extracting relevant features from the TF representation of the transient stator current that can be used for training neural networks, support vector machines and other automated expert systems.

34

Appendix A. Rated characteristics of motor A

Three-phase induction machine. $P = 1.1$ kW, $U = 230/400$ V, $I = 2.7/4.6$ A, $f = 50$ Hz, $n = 1410$ r/min, $\cos\varphi = 0.8$.

Appendix B. Rated characteristics of motor B

Three-phase induction machine. $P = 4$ kW, $U = 230/400$ V, $I = 4.65/8.06$ A, $f = 50$ Hz, $n = 1426$ r/min, $\cos\varphi = 0.85$.

References

[1] Y. Liu, A. M. Bazzi, A review and comparison of fault detection and diagnosis methods for squirrel-cage induction motors: State of the art, ISA Transactions 70 (2017) 400–409.

[2] S. K. Gundewar, P. V. Kane, Condition monitoring and fault diagnosis of induction motor in electric vehicle, in: R. Kumar, V. S. Chauhan, M. Talha, H. Pathak (Eds.), Machines, Mechanism and Robotics, Springer Singapore, Singapore (2022) 531–537.

[3] J. Faiz, S. Moosavi, Eccentricity fault detection – From induction machines to DFIG—A review, Renewable and Sustainable Energy Reviews 55 (2016) 169–179.

[4] J. Rangel-Magdaleno, H. Peregrina-Barreto, J. Ramirez-Cortes, I. Cruz-Vega, Hilbert spectrum analysis of induction motors for the detection of incipient broken rotor bars, Measurement 109 (2017) 247–255.

[5] Y. Wu, B. Jiang, Y. Wang, Incipient winding fault detection and diagnosis for squirrel-cage induction motors equipped on CRH trains, ISA Transactions 99 (2020) 488–495.

[6] J. R. Rivera-Guillen, J. De Santiago-Perez, J. P. Amezquita-Sanchez, M. Valtierra-Rodriguez, R. J. Romero-Troncoso, Enhanced FFT-based

method for incipient broken rotor bar detection in induction motors during the startup transient, Measurement 124 (2018) 277–285.

[7] C. Terron-Santiago, J. Martinez-Roman, R. Puche-Panadero, A. Sapena-Bano, A review of techniques used for induction machine fault modelling, Sensors 21 (14) (2021) 4855.

[8] S. Kumar, D. Mukherjee, P. K. Guchhait, R. Banerjee, A. K. Srivastava, D. N. Vishwakarma, R. K. Saket, A Comprehensive Review of Condition Based Prognostic Maintenance (CBPM) for Induction Motor, IEEE Access 7 (2019) 90690–90704.

[9] A. M. Alikhani, A. Vahedi, P. A. Khlyupin, Induction Motor Fault Detection in ESP Systems Based on Vibration Measurements, in: A. Ronzhin, V. Shishlakov (Eds.), Electromechanics and Robotics, Springer Singapore, Singapore (2022) 497–505.

[10] N. Cong-Phuong, Induction motor overload recognition based on sound analysis, in: Y.-D. Zhang, T. Senjyu, C. So-In, A. Joshi (Eds.), Smart Trends in Computing and Communications, Springer Singapore, Singapore (2022) 41–50.

[11] O. AlShorman, F. Alkahatni, M. Masadeh, M. Irfan, A. Glowacz, F. Althobiani, J. Kozik, W. Glowacz, Sounds and acoustic emission-based early fault diagnosis of induction motor: A review study, Advances in Mechanical Engineering 13 (2) (2021), `doi:10.1177/1687814021996915`.

[12] P. N. Phuc, D. Bozalakov, H. Vansompel, K. Stockman, G. Crevecoeur, Rotor Temperature Virtual Sensing for Induction Machines using a Lumped-Parameter Thermal Network and Dual Kalman Filtering, IEEE Transactions on Energy Conversion 36 (3) (2021) 1688–1699.

[13] F. Li, X. Pang, Z. Yang, Motor current signal analysis using deep neural networks for planetary gear fault diagnosis, Measurement 145 (2019) 45–54.

[14] M. Lopez-Ramirez, L. M. Ledesma-Carrillo, F. M. Garcia-Guevara, J. Munoz-Minjares, E. Cabal-Yepez, F. J. Villalobos-Pina, Automatic Early Broken-Rotor-Bar Detection and Classification Using Otsu Segmentation, IEEE Access 8 (2020) 112624–112632.

[15] Y. Guven, S. Atis, Implementation of an embedded system for real-time detection of rotor bar failures in induction motors, ISA Transactions 81 (2018) 210–221.

[16] I. Martin-Diaz, D. Morinigo-Sotelo, O. Duque-Perez, R. A. Osornio-Rios, R. J. Romero-Troncoso, Hybrid algorithmic approach oriented to incipient rotor fault diagnosis on induction motors, ISA Transactions 80 (2018) 427–438.

[17] M. Soualhi, K. T. Nguyen, A. Soualhi, K. Medjaher, K. E. Hemsas, Health monitoring of bearing and gear faults by using a new health indicator extracted from current signals, Measurement 141 (2019) 37–51.

[18] W. Oñate, Y. Gallardo, R. Pérez, G. Caiza, Comparative Analysis of High Frequencies for the Broken Bar Fault Diagnosis Using MCSA and Park's Vector Demodulation, in: Á. Rocha, C. H. Fajardo-Toro, J. M. R. Rodríguez (Eds.), Developments and Advances in Defense and Security, Springer Singapore, Singapore (2022) 119–130.

[19] A. Pilloni, A. Pisano, M. Riera-Guasp, R. Puche-Panadero, M. Pineda-Sanchez, Fault Detection in Induction Motors, in: AC Electric Motors Control, John Wiley & Sons Ltd, 2013, pp. 275–309.

[20] J. Penman, H. G. Sedding, B. A. Lloyd, W. T. Fink, Detection and location of interturn short circuits in the stator windings of operating motors, IEEE Trans. Energy Convers. 9 (4) (1994) 652–658.

[21] W. Deleroi, Broken bar in a squirrel-cage rotor of an induction-motor. 1. Description by superimposed fault-currents, Archiv fur Elektrotechnik 67 (2) (1984) 91–99.

37

[22] A. Bellini, F. Filippetti, G. Franceschini, C. Tassoni, G. Kliman, Quantitative evaluation of induction motor broken bars by means of electrical signature analysis, IEEE Transactions on Industry Applications 37 (5) (2001) 1248–1255.

[23] D. Dorrell, W. Thomson, S. Roach, Analysis of airgap flux, current, and vibration signals as a function of the combination of static and dynamic airgap eccentricity in 3-phase induction motors, IEEE Transactions on Industry Applications 33 (1) (1997) 24–34.

[24] T. Wang, G. Lu, P. Yan, A Novel Statistical Time-Frequency Analysis for Rotating Machine Condition Monitoring, IEEE Trans. Ind. Electron. 67 (1) (2020) 531–541.

[25] S. Esakimuthu Pandarakone, Y. Mizuno, H. Nakamura, A comparative study between machine learning algorithm and artificial intelligence neural network in detecting minor bearing fault of induction motors, Energies 12 (11) (2019) 2105.

[26] P. Vas, Parameter estimation, condition monitoring, and diagnosis of electrical machines, U.K., Oxford:Clarendon, 1993.

[27] L. Eren, M. Aşkar, M. J. Devaney, Motor current signature analysis via four-channel fir filter banks, Measurement 89 (2016) 322–327.

[28] Y. Zhang, K. Xing, R. Bai, D. Sun, Z. Meng, An enhanced convolutional neural network for bearing fault diagnosis based on time–frequency image, Measurement 157 (2020) 107667.

[29] J. Burriel-Valencia, R. Puche-Panadero, J. Martinez-Roman, A. Sapena-Bano, M. Pineda-Sanchez, J. Perez-Cruz, M. Riera-Guasp, Automatic Fault Diagnostic System for Induction Motors under Transient Regime Optimized with Expert Systems, Electronics 8 (1) (2018) 6.

[30] M. Singh, A. G. Shaik, Faulty bearing detection, classification and location in a three-phase induction motor based on stockwell transform and support vector machine, Measurement 131 (2019) 524–533.

[31] B. Yang, R. Liu, X. Chen, Fault Diagnosis for a Wind Turbine Generator Bearing via Sparse Representation and Shift-Invariant K-SVD, IEEE Trans. Ind. Informat. 13 (3) (2017) 1321–1331.

[32] M. Z. Ali, M. N. S. K. Shabbir, S. M. K. Zaman, X. Liang, Single- and Multi-Fault Diagnosis Using Machine Learning for Variable Frequency Drive-Fed Induction Motors, IEEE Trans. Ind Appl. 56 (3) (2020) 2324–2337.

[33] X. Dong, G. Li, Y. Jia, K. Xu, Multiscale feature extraction from the perspective of graph for hob fault diagnosis using spectral graph wavelet transform combined with improved random forest, Measurement 176 (2021) 109178.

[34] M. Pineda-Sanchez, M. Riera-Guasp, J. Perez-Cruz, R. Puche-Panadero, Transient motor current signature analysis via modulus of the continuous complex wavelet: A pattern approach, Energy Conversion and Management 73 (2013) 26–36.

[35] M. Riera-Guasp, M. Pineda-Sanchez, J. Perez-Cruz, R. Puche-Panadero, J. Roger-Folch, J. A. Antonino-Daviu, Diagnosis of Induction Motor Faults via Gabor Analysis of the Current in Transient Regime, IEEE Trans. Instrum. Meas. 61 (6) (2012) 1583–1596.

[36] J. Burriel-Valencia, R. Puche-Panadero, J. Martinez-Roman, A. Sapena-Bano, M. Pineda-Sanchez, Fault Diagnosis of Induction Machines in a Transient Regime Using Current Sensors with an Optimized Slepian Window, Sensors 18 (1) (2018) 146.

[37] X. Tu, Q. Zhang, Z. He, Y. Hu, S. Abbas, F. Li, Generalized Horizontal

39

Synchrosqueezing Transform: Algorithm and Applications, IEEE Trans. Ind. Electron. (2020) 5293–5302.

[38] X. Zhu, Z. Zhang, J. Gao, B. Li, Z. Li, X. Huang, G. Wen, Synchroextracting chirplet transform for accurate IF estimate and perfect signal reconstruction, Digital Signal Processing 93 (2019) 172–186.

[39] G. Yu, Y. Zhou, General linear chirplet transform, Mechanical Systems and Signal Processing 70-71 (2016) 958–973.

[40] W. Yang, P. J. Tavner, W. Tian, Wind Turbine Condition Monitoring Based on an Improved Spline-Kernelled Chirplet Transform, IEEE Trans. Ind. Electron. 62 (10) (2015) 6565–6574.

[41] K. Yu, T. R. Lin, H. Ma, H. Li, J. Zeng, A Combined Polynomial Chirplet Transform and Synchroextracting Technique for Analyzing Nonstationary Signals of Rotating Machinery, IEEE Trans. Instrum. Meas. 69 (4) (2020) 1505–1518.

[42] G. You, Y. Lv, Y. Jiang, C. Yi, A novel fault diagnosis scheme for rolling bearing based on convex optimization in synchroextracting chirplet transform, Sensors 20 (10) (2020) 2813.

[43] Z. Meng, M. Lv, Z. Liu, F. Fan, General synchroextracting chirplet transform: Application to the rotor rub-impact fault diagnosis, Measurement 169 (2021) 108523.

[44] X. Zhu, Z. Zhang, Z. Li, J. Gao, X. Huang, G. Wen, Multiple squeezes from adaptive chirplet transform, Signal Processing 163 (2019) 26–40.

[45] J. Luo, D. Yu, M. Liang, Application of multi-scale chirplet path pursuit and fractional Fourier transform for gear fault detection in speed up and speed-down processes, Journal of Sound and Vibration 331 (22) (2012) 4971–4986.

[46] J. Pons-Llinares, D. Morinigo-Sotelo, O. Duque-Perez, J. Antonino-Daviu, M. Perez-Alonso, Transient detection of close components through the chirplet transform: Rotor faults in inverter-fed induction motors, in: IECON 2014 - 40th Annual Conference of the IEEE Industrial Electronics Society, IEEE (2014) 3386–3392.

[47] V. Fernandez-Cavero, D. Morinigo-Sotelo, O. Duque-Perez, J. Pons-Llinares, A Comparison of Techniques for Fault Detection in Inverter-Fed Induction Motors in Transient Regime, IEEE Access 5 (2017) 8048–8063.

[48] S. Wei, D. Wang, Z. Peng, Z. Feng, Variational nonlinear component decomposition for fault diagnosis of planetary gearboxes under variable speed conditions, Mechanical Systems and Signal Processing 162 (2022) 108016.

[49] D. He, H. Cao, S. Wang, X. Chen, Time-reassigned synchrosqueezing transform: The algorithm and its applications in mechanical signal processing, Mechanical Systems and Signal Processing 117 (2019) 255–279.

[50] N. Holighaus, Z. Průša, P. L. Søndergaard, Reassignment and synchrosqueezing for general time–frequency filter banks, subsampling and processing, Signal Processing 125 (2016) 1 – 8.

[51] D. Camarena-Martinez, C. A. Perez-Ramirez, M. Valtierra-Rodriguez, J. P. Amezquita-Sanchez, R. de Jesus Romero-Troncoso, Synchrosqueezing transform-based methodology for broken rotor bars detection in induction motors, Measurement 90 (2016) 519–525.

[52] G. Yu, A Concentrated Time-Frequency Analysis Tool for Bearing Fault Diagnosis, IEEE Trans. Instrum. Meas. 69 (2) (2020) 371–381.

[53] L. Li, H. Cai, H. Han, Q. Jiang, H. Ji, Adaptive short-time Fourier transform and synchrosqueezing transform for non-stationary signal separation, Signal Processing 166 (2020) 107231.

[54] D. Zhang, Z. Feng, Enhancement of time-frequency post-processing readability for nonstationary signal analysis of rotating machinery: Princi-

ple and validation, Mechanical Systems and Signal Processing 163 (2022) 108145.

[55] Y. Qin, J. Zou, B. Tang, Y. Wang, H. Chen, Transient feature extraction by the improved orthogonal matching pursuit and K-SVD algorithm with adaptive transient dictionary, IEEE Trans. Ind. Informat. 16 (1) (2020) 215–227.

[56] M. Z. Ali, M. N. S. K. Shabbir, X. Liang, Y. Zhang, T. Hu, Machine Learning based Fault Diagnosis for Single- and Multi-Faults in Induction Motors Using Measured Stator Currents and Vibration Signals, IEEE Trans. Ind Appl. 55 (3) (2019) 2378 – 2391.

[57] M. A. Awal, S. Ouelha, S. Dong, B. Boashash, A robust high-resolution time–frequency representation based on the local optimization of the short-time fractional fourier transform, Digital Signal Processing 70 (2017) 125–144.

[58] M. Riera-Guasp, J. Antonino-Daviu, M. Pineda-Sanchez, R. Puche-Panadero, J. Perez-Cruz, A General Approach for the Transient Detection of Slip-Dependent Fault Components Based on the Discrete Wavelet Transform, IEEE Transactions on Industrial Electronics 55 (12) (2008) 4167–4180.

[59] Y. Xiao, Y. Hong, X. Chen, W. Chen, Y. Xiao, Y. Hong, X. Chen, W. Chen, The Application of Dual-Tree Complex Wavelet Transform (DTCWT) Energy Entropy in Misalignment Fault Diagnosis of Doubly-Fed Wind Turbine (DFWT), Entropy 19 (11) (2017) 587.

[60] S. N. Chegini, A. Bagheri, F. Najafi, Application of a new ewt-based denoising technique in bearing fault diagnosis, Measurement 144 (2019) 275–297.

[61] J. Burriel-Valencia, R. Puche-Panadero, J. Martinez-Roman, A. Sapena-Baño, M. Riera-Guasp, M. Pineda-Sánchez, Multi-band frequency window

for time-frequency fault diagnosis of induction machines, Energies 12 (17) (2019) 3361.

[62] B. E. Yousfi, A. Soualhi, K. Medjaher, F. Guillet, Electromechanical modeling of a motor–gearbox system for local gear tooth faults detection, Mechanical Systems and Signal Processing 166 (2022) 108435.

[63] S. Marmouch, T. Aroui, Y. Koubaa, Statistical neural networks for induction machine fault diagnosis and features processing based on principal component analysis, IEEJ Transactions on Electrical and Electronic Engineering 16 (2) (2021) 307–314.

[64] H. Talhaoui, T. Ameid, A. Kessal, Energy eigenvalues and neural network analysis for broken bars fault diagnosis in induction machine under variable load: experimental study, Journal of Ambient Intelligence and Humanized Computing (2021) 1–15.

[65] P. Kumar, A. S. Hati, Support vector classifier-based broken rotor bar detection in squirrel cage induction motor, in: R. Kumar, V. S. Chauhan, M. Talha, H. Pathak (Eds.), Machines, Mechanism and Robotics, Springer Singapore, Singapore, (2022), 429–438.

[66] D. Matić, F. Kulić, M. Pineda-Sánchez, I. Kamenko, Support vector machine classifier for diagnosis in electrical machines: Application to broken bar, Expert Systems with Applications 39 (10) (2012) 8681–8689.

[67] S. Bensaoucha, Y. Brik, S. Moreau, S. A. Bessedik, A. Ameur, Induction machine stator short-circuit fault detection using support vector machine, COMPEL-The international journal for computation and mathematics in electrical and electronic engineering, 40 (3) (2021) 373–389.

[68] W. Zhang, X. Li, Q. Ding, Deep residual learning-based fault diagnosis method for rotating machinery, ISA Transactions 95 (2019) 295–305.

[69] B. Yang, S. Xu, Y. Lei, C.-G. Lee, E. Stewart, C. Roberts, Multi-source transfer learning network to complement knowledge for intelligent diagnosis

of machines with unseen faults, Mechanical Systems and Signal Processing 162 (2022) 108095.

[70] S. Arena, E. Florian, I. Zennaro, P. Orrù, F. Sgarbossa, A novel decision support system for managing predictive maintenance strategies based on machine learning approaches, Safety Science 146 (2022) 105529.

[71] L. C. Brito, G. A. Susto, J. N. Brito, M. A. Duarte, An explainable artificial intelligence approach for unsupervised fault detection and diagnosis in rotating machinery, Mechanical Systems and Signal Processing 163 (2022) 108105.

[72] W. Zhang, X. Li, X.-D. Jia, H. Ma, Z. Luo, X. Li, Machinery fault diagnosis with imbalanced data using deep generative adversarial networks, Measurement 152 (2020) 107377.

[73] T. Yan, D. Wang, M. Zheng, T. Xia, E. Pan, L. Xi, Fisher's discriminant ratio based health indicator for locating informative frequency bands for machine performance degradation assessment, Mechanical Systems and Signal Processing 162 (2022) 108053.

[74] P. Gangsar, Z. Ali, M. Chouksey, A. Parey, An intelligent and robust fault diagnostics for an electromechanical system using vibration and current signals, in: S. K. Natarajan, R. Prakash, K. Sankaranarayanasamy (Eds.), Recent Advances in Manufacturing, Automation, Design and Energy Technologies, Springer Singapore, Singapore (2022) 485–494.

[75] Y. Abdoush, G. Pojani, G. E. Corazza, Adaptive Instantaneous Frequency Estimation of Multicomponent Signals Based on Linear Time-Frequency Transforms, IEEE Trans. Signal Process. 67 (12) (2019) 3100–3112.

[76] D. Gabor, Theory of communication. part 1: The analysis of information, Journal of the Institution of Electrical Engineers - Part III: Radio and Communication Engineering 93 (1946) 429–441.

[77] B. Huang, G. Feng, X. Tang, J. X. Gu, G. Xu, R. Cattley, F. Gu, A. D. Ball, A performance evaluation of two bispectrum analysis methods applied to electrical current signals for monitoring induction motor-driven systems, Energies 12 (8) (2019) 1438.

[78] S. Chen, X. Dong, Y. Yang, W. Zhang, Z. Peng, G. Meng, Chirplet Path Fusion for the Analysis of Time-Varying Frequency-Modulated Signals, IEEE Trans. Ind. Electron. 64 (2) (2017) 1370–1380.

[79] J. Burriel-Valencia, R. Puche-Panadero, J. Martinez-Roman, A. Sapena-Bano, M. Pineda-Sanchez, Short-Frequency Fourier Transform for Fault Diagnosis of Induction Machines Working in Transient Regime, IEEE Trans. Instrum. Meas. 66 (3) (2017) 432–440.

[80] A. Sapena-Bano, M. Pineda-Sanchez, R. Puche-Panadero, J. Martinez-Roman, D. Matic, Fault Diagnosis of Rotating Electrical Machines in Transient Regime Using a Single Stator Current's FFT, IEEE Trans. Instrum. Meas. 64 (11) (2015) 3137–3146.

[81] A. Tavighi, H. Ahmadi, M. Armstrong, J. R. Martí, Discrete-time fourier series to simulate transient over voltages in power systems, Electric Power Systems Research 188 (2020) 106529.

[82] M. Cabanas, J. Ruiz Gonzalez, J. Sampayo, M. Melero, C. Rojas, F. Pedrayes, A. Arguelles, J. Vina, Analysis of the fatigue causes on the rotor bars of squirrel cage asynchronous motors: experimental analysis and modelling of medium voltage motors, in: 4th IEEE International Symposium on Diagnostics for Electric Machines, Power Electronics and Drives, 2003. SDEMPED 2003, (2003) 247–252.

[83] I. Culbert, J. Letal, Signature analysis for online motor diagnostics: Early detection of rotating machine problems prior to failure, IEEE Industry Applications Magazine 23 (4) (2017) 76–81.

[84] V. Fernandez-Cavero, L. A. García-Escudero, J. Pons-Llinares, M. A. Fernández-Temprano, O. Duque-Perez, D. Morinigo-Sotelo, Diagnosis of broken rotor bars during the startup of inverter-fed induction motors using the dragon transform and functional ANOVA, Applied Sciences 11 (9) (2021) 3769.

[85] F. F. Costa, L. A. L. de Almeida, S. R. Naidu, E. R. Braga-Filho, Improving the signal data acquisition in condition monitoring of electrical machines, IEEE Trans. Instrum. Meas. 53 (4) (2004) 1015–1019.

[86] D. A. Elvira-Ortiz, D. Morinigo-Sotelo, A. L. Zorita-Lamadrid, R. A. Osornio-Rios, R. de J. Romero-Troncoso, Fundamental Frequency Suppression for the Detection of Broken Bar in Induction Motors at Low Slip and Frequency, Applied Sciences 10 (12) (2020) 4160.

[87] A. Sapena-Bano, J. Burriel-Valencia, M. Pineda-Sanchez, R. Puche-Panadero, M. Riera-Guasp, The Harmonic Order Tracking Analysis Method for the Fault Diagnosis in Induction Motors Under Time-Varying Conditions, IEEE Transactions on Energy Conversion 32 (1) (2017) 244–256.

[88] R. Puche-Panadero, J. Martinez-Roman, A. Sapena-Bano, J. Burriel-Valencia, M. Riera-Guasp, Fault diagnosis in the slip–frequency plane of induction machines working in time-varying conditions, Sensors 20 (12) (2020) 3398.

[89] A. Sapena-Bano, J. Martinez-Roman, R. Puche-Panadero, M. Pineda-Sanchez, J. Perez-Cruz, M. Riera-Guasp, Induction machine model with space harmonics for the diagnosis of rotor eccentricity, based on the convolution theorem, International Journal of Electrical Power and Energy Systems 117 (2020) 105625.

[90] F. Vedreño-Santos, M. Riera-Guasp, H. Henao, M. Pineda-Sánchez, Diagnosis of faults in induction generators under fluctuating load conditions

through the instantaneous frequency of the fault components, in: 2012 XXth International Conference on Electrical Machines (2012) 1653–1659.

[91] J. Pons-Llinares, J. A. Antonino-Daviu, M. Riera-Guasp, M. Pineda-Sanchez, V. Climente-Alarcon, Induction Motor Diagnosis Based on a Transient Current Analytic Wavelet Transform via Frequency B-Splines, IEEE Trans. Ind. Electron. 58 (5) (2011) 1530–1544.

47